THE ASTROPHYSICAL JOURNAL, 376:150–160, 1991 July 20

THE MULTIPLE-SHELL STRUCTURE OF THE PLANETARY NEBULA NGC 6751[1]

YOU-HUA CHU[2]
Astronomy Department, University of Illinois, 1002 W. Green Street, Urbana, IL 61801
ARTURO MANCHADO
Instituto de Astrofisica de Canarias, E-38200 La Laguna, Spain
GEORGE H. JACOBY
Kitt Peak National Observatory, P.O. Box 26732, Tucson, AZ 85726
AND
KAREN B. KWITTER
Astronomy Department, Williams College, Williamstown, MA 01267
Received 1990 September 28; accepted 1991 January 21

ABSTRACT

An intriguing bipolar mass outflow and a faint envelope were detected spectroscopically in the planetary nebula NGC 6751 by Gieseking & Solf. To study the physical structure, we have obtained deep CCD images of this nebula, which detect not only the morphological counterparts of the aforementioned features but also additional faint halos extending out to a much larger radius.

We have further obtained long-slit echelle spectra to determine the internal motion and radial velocity, and low-dispersion spectra to determine the physical condition and abundances of each feature in the whole nebula. NGC 6751 is apparently a multiple-shell nebula moving through a gas-rich environment. We find an He abundance difference between the planetary nebula and the ambient medium; we also find an N/O abundance ratio enhancement in the [N II]–bright knots in the main nebula. From the physical structure of the shells in NGC 6751 we derive information about the average mass-loss rates at various stages.

Subject headings: nebulae: individual (NGC 6751) — nebulae: internal motions — nebulae: planetary — nebulae: structure

1. INTRODUCTION

The planetary nebula (PN) NGC 6751 had not attracted much attention until Gieseking & Solf (1986, hereafter GS) discovered spectroscopically a bipolar mass outflow and a faint static envelope outside the bright main nebula, while neither system was registered in the only photograph (Duncan 1937) available to GS. The CCD image published by Chu, Jacoby, & Arendt (1987, hereafter CJA) did show two ansae corresponding to the bipolar outflow, but the faint envelope was still not detected.

Intrigued by GS's discovery, we have included NGC 6751 in our observing program for multiple-shell PNs. Our new deep-exposure CCD images show clearly not only all the systems detected by GS but also additional faint filaments extending out to a radius greater than 100″, four times at extended as the static envelope. These faint filaments have also been detected by Hua & Louise (1990). Using the radial velocities derived from the follow-up echelle observations, we find that some of the outer filaments belong to a halo of NGC 6751, while others are the ambient interstellar material ionized by the central star of NGC 6751. NGC 6751 is apparently a triple-shell nebula moving through a gas-rich environment.

The multiple-shell phenomenon is prevalent in PNs; however, hardly any nebula has more than three visible shells (CJA). Even triple-shell nebulae are rare; only seven are known: NGC 2022, NGC 6720, NGC 6751, NGC 6826, NGC 6891, NGC 7662, and A78 (CJA; Moreno & López 1987; Manchado, Pottasch, & Mampaso 1988; this paper). The triple-shell nebulae provide a unique opportunity to examine an extended history of the stellar mass loss, since each shell presumably marks an era with a distinct mode or rate of mass loss. It is important to study each triple-shell nebula. Furthermore, it is important to study the kinematics and physical conditions of each shell in order to determine the characteristics of the mass loss and the formation mechanism of the shells. The chemical abundances in each shell reflect the condition of the atmosphere of the central star at the time of the mass loss. To supplement the existing single-aperture spectroscopic study of NGC 6751 (Aller & Czyzak 1983), we have obtained low-dispersion, long-slit spectra of NGC 6751 so that its complex features can be resolved and studied differentially.

In this paper we report the results of our imagery and high- and low-dispersion spectroscopic studies of the triple-shell nebula NGC 6751. The observations are described in § 2. The morphology, kinematic properties, and physical conditions and abundances are reported in §§ 3, 4, and 5, respectively. Finally we discuss the mass-loss and formation mechanism of NGC 6751 and its interaction with the ambient interstellar medium in § 6.

2. OBSERVATIONS AND DATA REDUCTION

2.1. *Imagery*

The CCD images of NGC 6751 were obtained with the 2.1 m telescope at Kitt Peak National Observatory (KPNO) on 1986 September 21. A 512 × 512 Tektronix CCD was used. The

[1] Based on observations collected at the Kitt Peak National Observatory and at the European Southern Observatory, La Silla, Chile.

[2] Visiting Astronomer, Kitt Peak National Observatory, National Optical Astronomy Observatories, which is operated by the Associated Universities for Research in Astronomy, Inc., under contract with the National Science Foundation.

TABLE 1A

IMAGES OF NGC 6751

Number	Nebular Line	Filter λ, Δλ (Å)	Exposure Time (minutes)
1	Hα	6563, 11	5
2	[O III]	5004, 27	5
3	[N II]	6585, 15	10
4	[N II]	6585, 15	5

TABLE 1B

ECHELLE OBSERVATIONS OF NGC 6751

Number	Offset from Central Star	Position Angle	Exposure Time (minutes)
1	...	105°	30
2	...	0	20
3	35″ W	0	20
4	38″ E, 52″ N	0	20

TABLE 1C

LOW-RESOLUTION SPECTROSCOPY OF NGC 6751

Number	Offset from Central Star	Position Angle	Exposure Time (minutes)
1	...	104°	10
2	19″ W	34.5	60

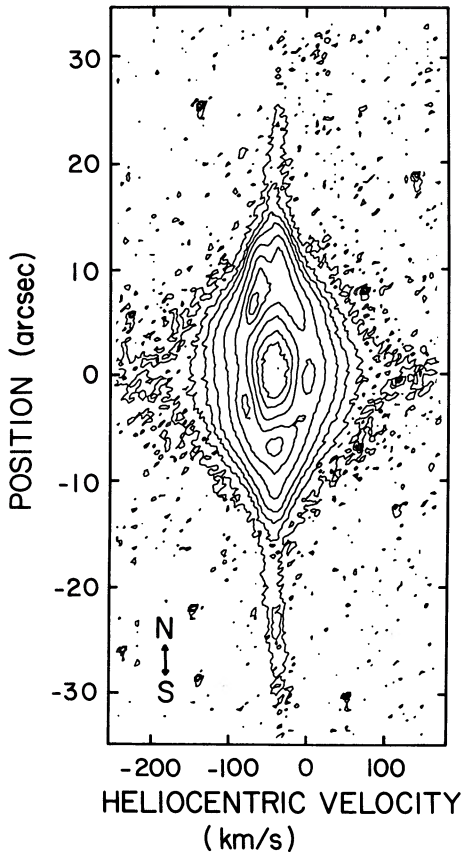

FIG. 4.—Contour map of the echellogram displayed in Fig. 3*b*. The contour levels are at 90%, 75%, 50%, 25%, 10%, 5%, 2.5%, and 1% of the peak value, 818 counts.

pixel size was 27 μm, corresponding to 0″.35. The field of view was 3′. The low readout noise (6 electrons) of the Tektronix CCD made it possible to detect faint nebulosity even in short exposure times. Four images through interference filters were obtained. See Table 1A for the filter characteristics and exposure times.

The central 80″ × 80″ of the first three images are reproduced in Figure 1 (Plate 1). Each image is displayed at four levels to accentuate the bright (*top panel*) and faint (*bottom panel*) features. The Hα, [N II] and [O III] full-frame images are reproduced in Figure 2 (Plate 2) to show the faint outer filaments. The last image, a shorter exposure in [N II], was taken with a 30″ south offset from the position of the other three images to look for counterparts of the northwest irregular filaments in the southwest quadrant; however, no additional nebulosity is seen.

2.2. *Echelle Observations*

A direct way to determine the relationship among the morphological features in a nebula is through the kinematics, which can be studied with high-dispersion spectroscopy. Therefore, we obtained four long-slit spectra of NGC 6751 with the echelle spectrograph on the 4 m telescope at KPNO on 1987 September 1–2.

We used a 79 line mm^{-1} echelle grating and the long-focus camera. The resulting reciprocal dispersion was 2.47 Å mm^{-1} at 5000 Å. The UV flooded 800 × 800 T12 CCD was used with 2 × 2 binning, and the resulting pixel size (30 μm) was equivalent to ~4.5 km s^{-1} along the dispersion and 0″.33 perpendicular to the dispersion. The instrumental FWHM is 9.3 ± 0.3 km s^{-1}. The spectra were taken in the [O III] line to minimize the intrinsic thermal widths and to avoid the contamination of telluric lines. The slit positions, orientations, and exposure times are given in Table 1B.

The slit positions are also shown in Figure 2*c*. The images of the spectra are reproduced in Figure 3 (Plate 3). The first two spectra were displayed twice to show the bright inner nebula and the faint outer part, respectively. A contour map of the second echelle line image is presented in Figure 4. Several representative line profiles are plotted in Figure 5.

2.3. *Low-Dispersion Spectroscopic Observations*

In order to investigate the physical condition of the ionized gas in the central nebula as well as in the halo, low-dispersion long-slit spectroscopy was conducted using the ESO Faint Object Spectrograph and Camera (EFOSC; Dekker & D'Odorico 1985) on the ESO 3.6 m telescope at La Silla in 1988 March. The slit used was 0″.5 wide and 3′ long. The blue 300 grism gives a reciprocal dispersion of 230 Å mm^{-1} and an effective resolution of 4.1 Å. The data were recorded with the ESO CCD 11 chip in 1030 × 160 arrays, with the long dimension along the dispersion and the short in the spatial direction. The pixel size is 15 μm by 60 μm, corresponding to 3.45 Å by 1″.35. The seeing was about 1″.6.

Two slit positions, shown in Figure 2*c*, were taken to cover the bright central nebula and the faint outer halos, respectively. The first slit position was selected to cover both the central nebula and the ansae that correspond to GS's bipolar outflow.

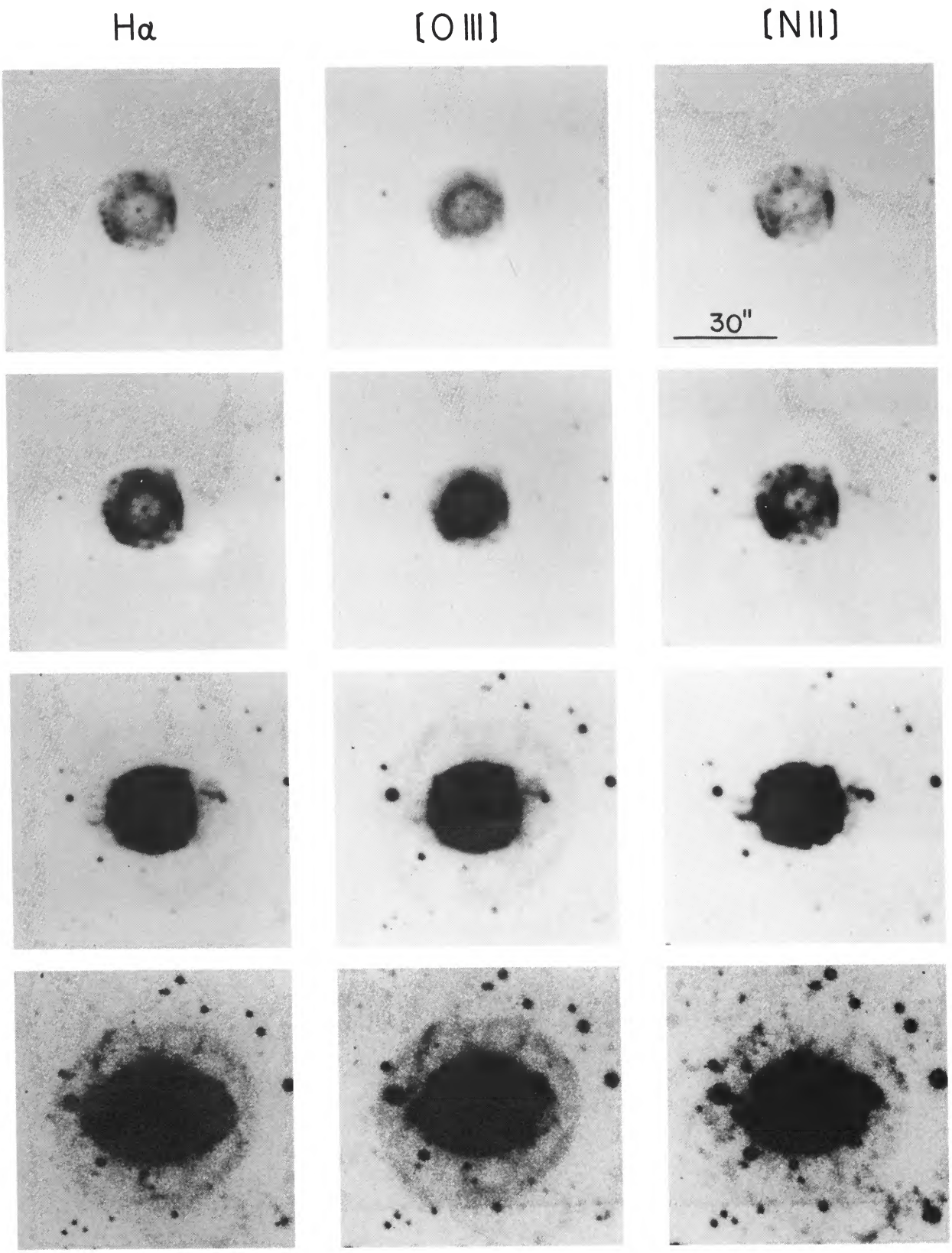

FIG. 1.—CCD images of NGC 6751 in the Hα, [O III], and [N II] lines, displayed at four levels of intensity. North is at the top, and east is to the left.

CHU, MANCHADO, JACOBY, & KWITTER (see 376, 151)

PLATE 2

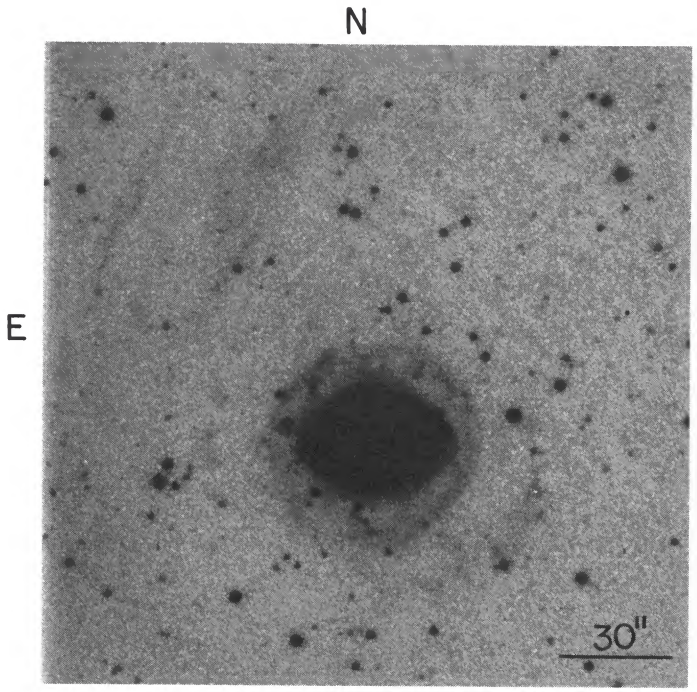

FIG. 2*a*

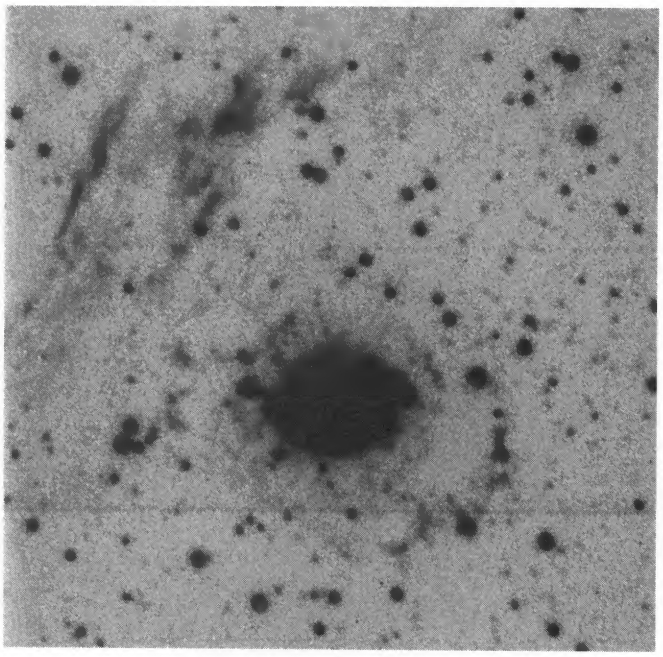

FIG. 2*b*

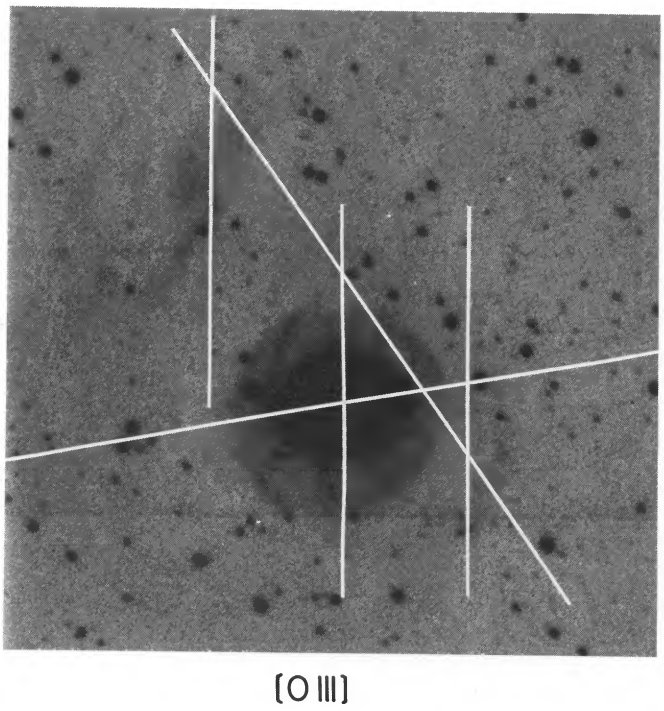

FIG. 2*c*

FIG. 2.—(*a*) Hα image of NGC 6751. North is at the top, and east is to the left. (*b*) [N II] image of NGC 6751. (*c*) [O III] image of NGC 6751. The slit positions of the high- and low-resolution spectra are shown.

CHU, MANCHADO, JACOBY, & KWITTER (see 376, 151)

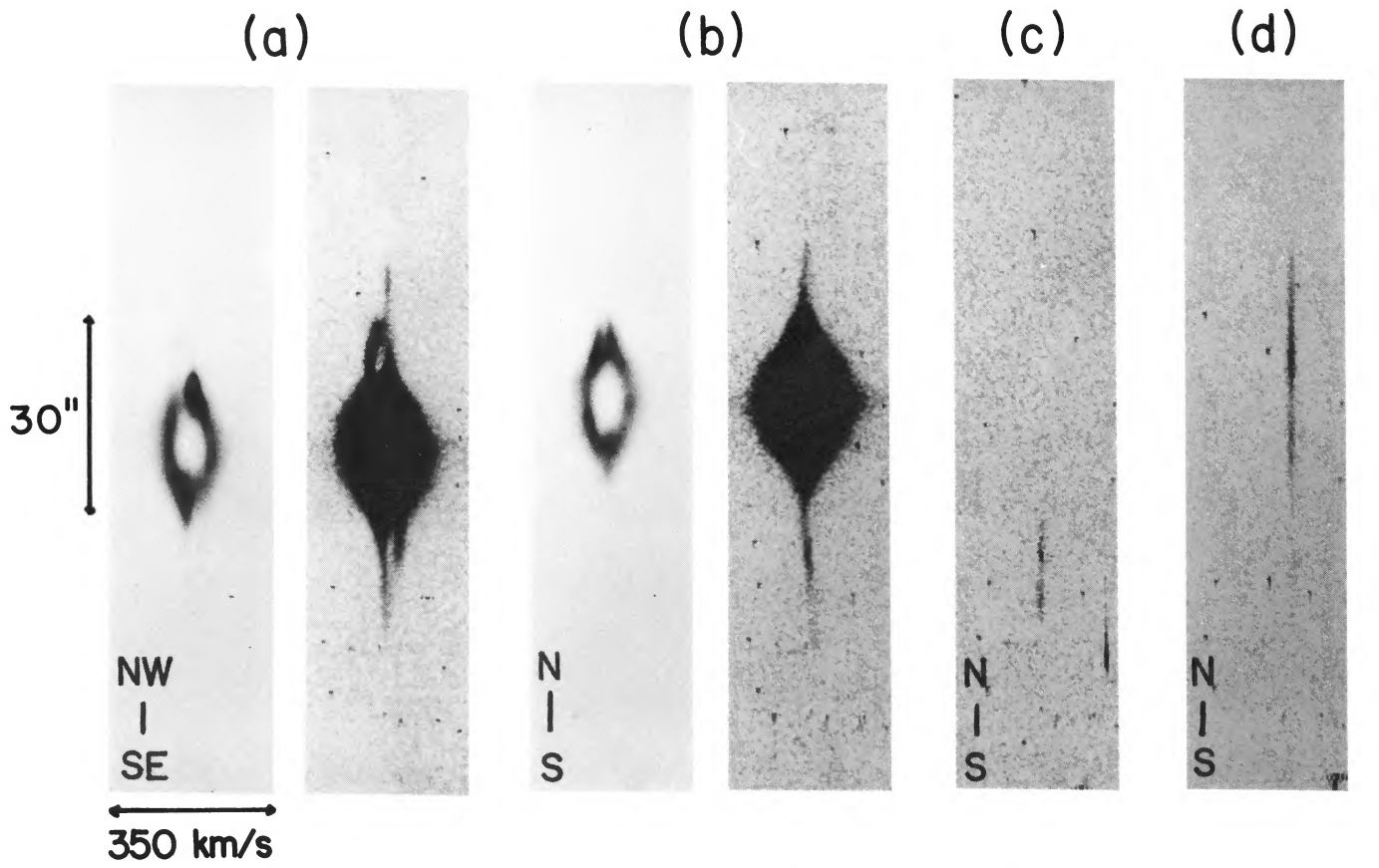

FIG. 3.—[O III] echellograms of NGC 6751. Every panel covers about 350 km s^{-1} with the same beginning and ending velocities. (*a*) Slit centered on the central star, at a position angle of 105°. The echellogram is displayed in two intensity levels to show the bright inner nebula and the fainter envelope and ansae. (*b*) Slit centered on the central star along the north-south direction. The echellogram was displayed at two intensity levels to show the bright inner nebula and the faint envelope. (*c*) Slit position, having a 35″ offset from the central star, centered on the faint halo. (*d*) Slit position, having a offset of 38″ east and 52″ north from the central star, centered on the irregular filaments in the northeast.

CHU, MANCHADO, JACOBY, & KWITTER (see 376, 151)

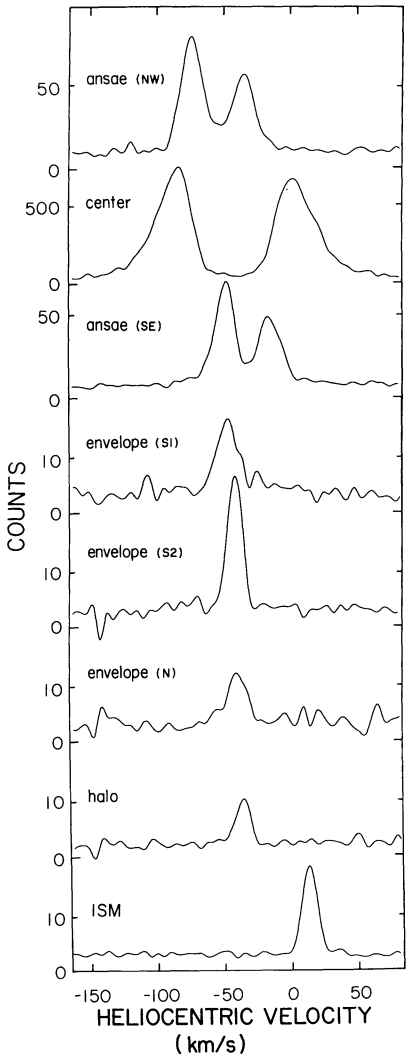

FIG. 5.—High-resolution line profiles at selected positions. The slit position and size (offset from central star, slit length) of these spectra are (13".9 SE, 2".3), ([no offset], 1"), (16".3 SE, 4"), (18".3 S, 4"), (24".3 S, 3".3), (22".3 N, 3".3), (43" SW, 7".6), (67" NE, 27").

The second slit position was selected to cover the static envelope, the outer halo, and the irregular filaments in the northeast. Table 1C gives the offset and position angle of the slit positions and the exposure times.

3. MORPHOLOGY OF NGC 6751

The structure of NGC 6751 is complex. There are six apparent morphological features in Figures 1 and 2. In order of increasing radius, or decreasing surface brightness, these features are (1) the bright circular main nebula with 25" diameter, (2) a pair of 6" long ansae protruding from the main nebula at position angles of 104° and 284°, (3) an approximately east-west–oriented 42" × 28" oval enclosing the inner nebula and the ansae, (4) a faint 62" × 54" envelope, (5) a faint incomplete knotty ring at a radius of ~46", and (6) faint irregular filaments extending to 105" radius in the northeast quadrant. These features are individually described below.

The circular main nebula (see top panels of Fig. 1) actually consists of a smooth inner ring (16" across) and a knotty outer ring (25" across). The knots in the outer ring are most conspicuous in the low-excitation line of [N II]. The [O III] surface brightness decreases outward with little perturbation from the [N II]–bright knots. As we shall show later, this contrast between the [O III] and [N II] images probably manifests more than just ionization and excitation stratifications in a nebula.

The ansae (see the middle two rows of pictures in Fig. 1) are curved and knotty. These ansae are at the same location where GS detected the bipolar outflow. Note that the brightest "knot" at the western tip of the ansae is a foreground star. The ansae are enclosed in an oval (see the bottom panels in Fig. 1) aligned along a similar direction to the ansae. It is not clear whether the ansae and the oval belong to the same system, with the ansae being the condensations in the oval.

The faint envelope (see the bottom panels in Fig. 1) is limb-brightened and has radial filaments in both Hα and [O III] lines. It appears patchier in the [N II] line. The size of this envelope is identical to the static envelope detected spectroscopically by GS.

In Figure 2 there are still faint nebulosities outside the envelope. These nebulosities can be separated into two distinct groups according to location, morphology, and spectroscopic behavior. One group consists of the ring of knotty material located at ~46" from the central star of NGC 6751; these knots are best seen in the sectors northeast-east-southeast and west-southwest-south. The other group consists of the fainter, irregular filaments in the northeast quadrant at a larger distance, about 60"–100" from the central star. The [N II]/Hα line intensity ratios in both groups are significantly higher than those in the envelope.

4. KINEMATIC PROPERTIES OF NGC 6751

All six morphologically identified systems were sampled in the echelle observations. Although the coverage is not adequate to allow three-dimensional spatiokinematic modeling, the internal motion can be well diagnosed from the velocity dispersions and the radial velocities.

The main nebula shows a bow-shaped line image, indicating an expanding-shell structure. The peak-to-peak line split is 85 ± 2 km s^{-1}, which is traditionally interpreted as an expansion velocity of 42.5 km s^{-1}. However, the shell is not expanding at a uniform velocity, since the intrinsic velocity dispersion (after correcting for instrumental and thermal broadenings) in the shell is large, FWHM $= 28 \pm 3$ km s^{-1}. The velocity profile extracted near the nebular center (see Fig. 5) is asymmetric—steeper toward the systemic velocity. These velocity structures most likely result from a velocity gradient or a large amount of turbulence within the shell. To distinguish between these two possibilities, one needs to map the velocity structure over the entire main nebula and compare it with models of an expanding shell with built-in velocity gradient. Additional constraints can be provided by the expected symmetry in the nebula.

The knotty outer ring (25" across) in the main nebula may not follow the expansion pattern of the aforementioned shell. These knots are at the periphery of the main nebula, where the expansion is mostly tangential to the line of sight and the emission line should appear near the systemic velocity; nevertheless, the knots appear as bright blobs at higher radial velocities, giving the bow-shaped line image a tilted look (Fig. 3*a*) or a double-horned impression (Fig. 3*b*). This phenomenon is seen in other planetaries, such as NGC 3242, NGC 6826, NGC 7009, and NGC 7662 (Balick, Preston, & Icke 1987). It is pos-

sible that these knots expand faster than the shell; however, we note that the velocity anomaly can also be caused by purely geometric projection effect. For example, if the knots are located in an inclined equatorial band within a thick shell with built-in velocity gradient, this configuration may explain the observed radial velocities. A complete mapping of the velocity field in the nebula can place more constraints on this ambiguity.

The ansae, corresponding to GS's bipolar outflow, appear curved in the line image. Like the knotty ring, the interpretation depends on the three-dimensional geometry of the ansae; the curvature of the line image may indicate a real deceleration of expansion velocity at larger radius or the projection of a curved filament with a uniform expansion velocity. It is interesting to note that in the echelle line image the ansae protrude from the faintest part of the inner ring. It is not clear whether this anticorrelation in intensity has any physical significance.

The east-west–oriented 42″ × 28″ oval does not have a distinct velocity feature; it appears as an extension of the main nebula at the systemic velocity. The line broadening in the oval indicates an expansion. Our slit positions are either along the shorter axis of the oval, where the oval is not much more extended than the main nebula, or along the longer axis, where the ansae dominate the emission. Not much information about the oval can be derived from our spectra.

The static envelope detected by GS is clearly detected in our echellograms. The observed line widths extracted at 18″ south, 24″ south, 22″ north, 22″ southeast, and 26″ northwest from the central star are 19.4, 13.4, 16.8, 14.1, and 12.6 km s^{-1}, respectively. The anticorrelation between the line width and the radius, broader line profiles at smaller radii, can be explained by a slow expansion. After correcting for the instrumental profile and thermal broadening, we derive an expansion velocity of 10 ± 1 km s^{-1} for this 62″ × 54″ envelope.

The third echelle observation was taken on the faint knotty ring at 46″ radius. The line is narrow with an observed FWHM of 12.7 km s^{-1}, corresponding to an intrinsic turbulent FWHM of 6.2 km s^{-1}. The slit position is near the periphery of the ring, where we benefit from the higher surface brightness but lose some accuracy in determining the expansion velocity. The ring is detected for about 15″ along the slit, of which the distance to the central star ranges from 41″ to 46″. Assuming that the FWHM of 6.2 km s^{-1} is due to the expansion projected to the line of sight at 41″ to the star, then the expansion velocity can be approximated as (FWHM/2) × {sin [$\cos^{-1}$ (41/46)]} = 7 ± 2 km s^{-1}. The larger error is due to the uncertainty in the geometric correction.

Finally, the last slit position was chosen to cover the irregular filaments at the northeast quadrant. The extracted line profiles are narrow, with an observed FWHM of 13.8 km s^{-1}, corresponding to an intrinsic turbulent FWHM of 8.2 km s^{-1}. This component is unlikely to be part of NGC 6751 because of the large difference in radial velocity. The heliocentric velocity (V_{hel}) of this component is 13 ± 1 km s^{-1}, while that of the main nebula of NGC 6751 is −42 ± 2 km s^{-1}. Although a large velocity difference between a main nebula and its halo has been seen in the Helix nebula (Walsh & Meaburn 1987), the lack of velocity profile variation at different distances to the central star makes it unlikely that the irregular filaments are part of the planetary nebula NGC 6751. These irregular filaments probably have an interstellar origin; they would be an H II region ionized by the central star of NGC 6751.

5. PHYSICAL CONDITIONS OF THE IONIZED GAS

5.1. *Extraction of Spectral Line Strengths*

To determine the spatial extents over which spectra could be averaged, we first inspected the spectra visually line by line along the slit, then grouped together the adjacent spectra that shared similar spectral characteristics. Eight spectra, referred to as CS, C1, C2, A, E, H, H′, and F, were extracted; their spatial extents are 8.″1, 10.″8, 10.″8, 8.″1, 21.″6, 4.″0, 4.″0, and 9.″5, respectively. The locations of these spectra are labeled against the Hα surface brightness profiles in Figure 6. Compared with the morphological features defined in § 3, CS is centered on the central star, C1 is the smooth ring in the main nebula, C2 the knotty outer ring in the main nebula, A the ansae on both sides, E the envelope, H the faint halo at the southwest, H′ the faint halo at the north, and F the irregular filaments in the northeast. The spectra are shown in Figure 7.

The extinction is determined from the Balmer decrement (Hα, Hβ, and Hγ lines) in the main nebula, since its spectra have the highest signal-to-noise ratio. The extinction derived from the Hα/Hβ ratio (E_{B-V} = 0.45) is slightly lower than that

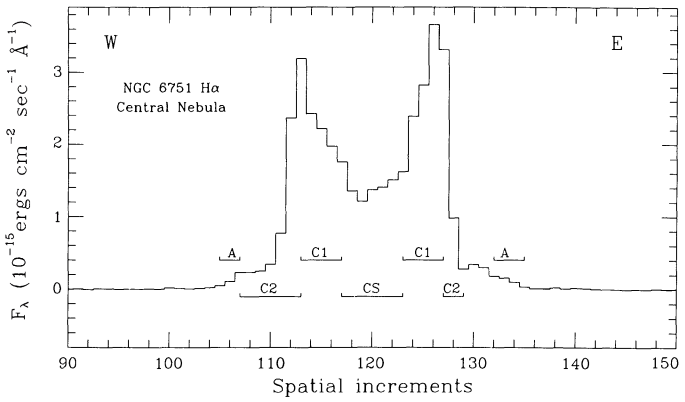

FIG. 6a

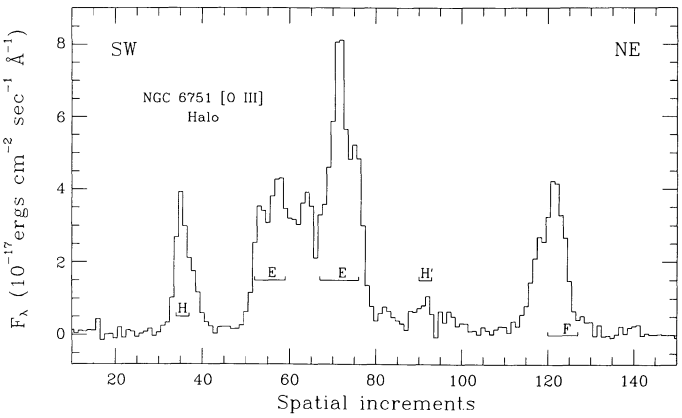

FIG. 6b

FIG. 6.—Surface brightness profiles extracted from the low-dispersion spectra. The effective slit positions for the extracted spectra are labeled below the profiles. (*a*) Hα line along the slit passing through the central star. (*b*) [O III] line along the slit passing through the envelope and halo of NGC 6751 and the irregular filaments in the northeast. See Fig. 2*c* for the slit position.

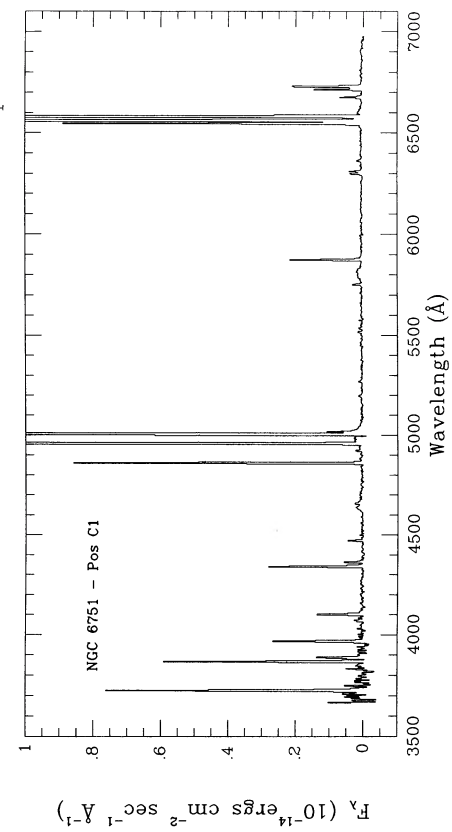

FIG. 7b

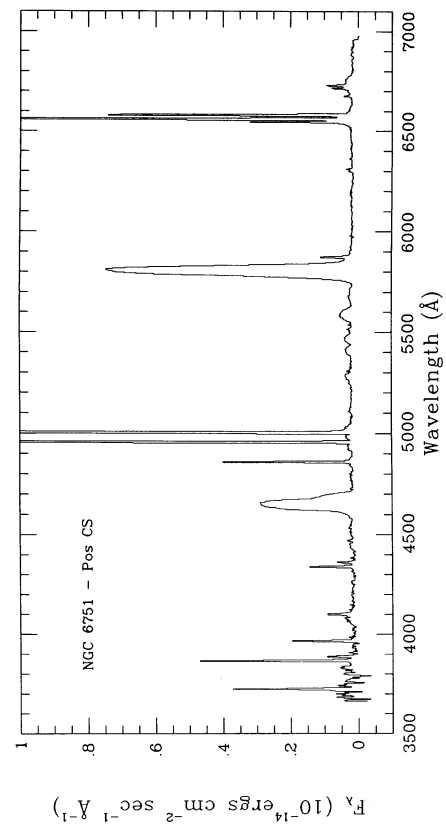

Fig. 7a

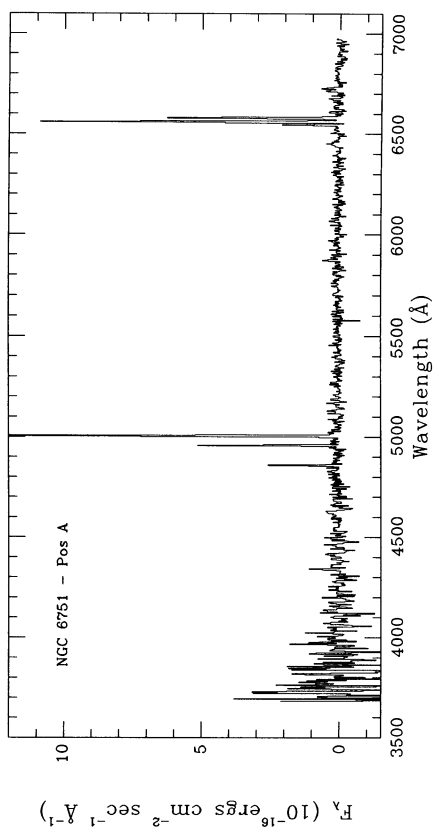

FIG. 7d

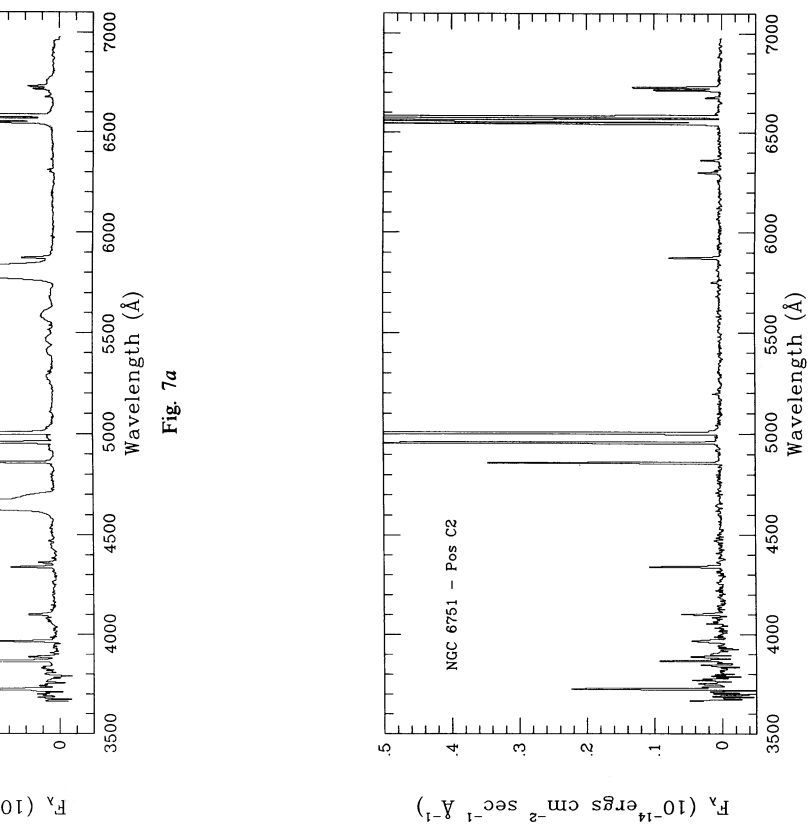

FIG. 7c

FIG. 7.—Low-resolution spectra of NGC 6751, (*a*) at position CS, (*b*) at C1, (*c*) at C2, (*d*) at A, (*e*) at E, (*f*) at H, and (*g*) at F

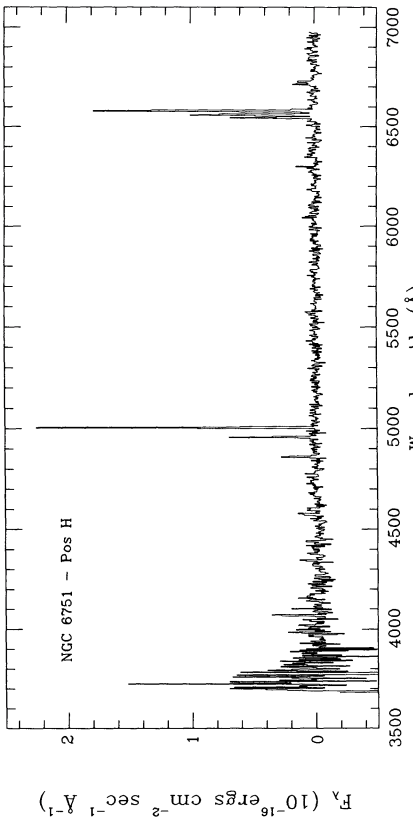

FIG. 7*f*

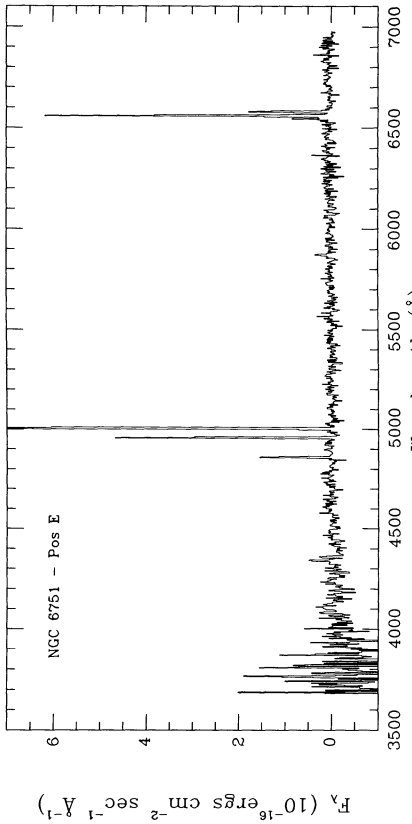

FIG. 7*e*

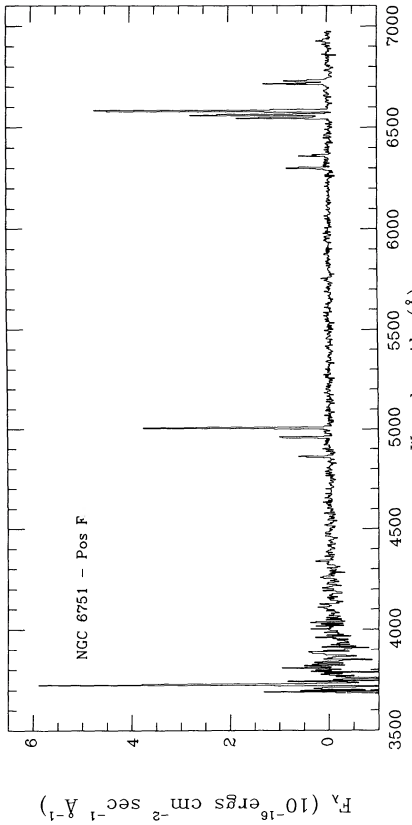

FIG. 7*g*

TABLE 2

LINE INTENSITY RATIOS FOR NGC 6751

Line	$f(\lambda)$	CS	C1	C2	A	E	H	H′	F
[O II] λ3727	0.26	153 ± 7	157 ± 7	125 ± 8	484:	...	326 ± 60	15 ± 4	1212 ± 100
[Ne III] λ3869	0.23	185 ± 30	98 ± 5	38 ± 6	...	...	...	...	...
H8 λ3889	0.22	33 ± 5	27 ± 4	21 ± 8	...	...	...	...	...
[Ne III], Hε λ3969	0.21	76 ± 4	47 ± 3	32 ± 9	...	...	...	...	...
[S II] λ4070	0.18	...	3.9 ± 0.4	...	...	...	211 ± 60	...	...
Hδ λ4101	0.18	31 ± 6	25 ± 4	25 ± 5	...	...	...	...	...
Hγ λ4340	0.135	50 ± 4	46 ± 4	42 ± 2	50 ± 10	38 ± 8	...	...	42 ± 8
[O III] λ4363	0.13	18 ± 3	8.5 ± 1	2.0 ± 0.6	20:	35 ± 10	...	...	...
He I λ4471	0.10	1.8 ± 0.8	6 ± 1	...	...	...	...	...	...
Hβ λ4861	0.00	100 ± 2	100 ± 2	100 ± 2	100 ± 15	100 ± 5	100 ± 8	100 ± 30	100 ± 10
[O III] λ4959	−0.02	606 ± 1	381 ± 6	191 ± 4	213 ± 10	345 ± 3	211 ± 4	140 ± 42	166 ± 10
[O III] λ5007	−0.03	1832 ± 1	1118 ± 10	595 ± 6	676 ± 20	1051 ± 10	702 ± 14	554 ± 25	553 ± 12
[N I] λ5199	−0.08	...	1.7 ± 3	2.2 ± 0.4	...	...	...	...	...
[Fe III] λ5270	−0.09	...	0.87 ± 0.4	...	...	...	...	...	...
[Fe III] λ5412	−0.12	...	2.2 ± 0.3	...	...	...	...	...	...
[Cl III] λ5515	−0.15	...	0.67 ± 0.3	...	...	...	...	...	...
[Cl III] λ5537	−0.15	...	0.74 ± 0.3	...	...	...	...	...	...
[N II] λ5755	−0.21	...	2.1 ± 0.3	2.3 ± 0.4	...	5.45:	6.36 ± 3	...	11.4 ± 3.4
He I λ5876	−0.23	18.2 ± 1.8	17.5 ± 0.8	18 ± 1	19 ± 6	21.62:	...	...	9.3 ± 3
[O I] λ6300	−0.30	2.3 ± 0.8	3.0 ± 0.4	5.9 ± 1	...	...	...	...	84 ± 8
[S III] λ6312	−0.30	2.8 ± 0.8	3.1 ± 0.4	4.0 ± 1	...	...	...	...	...
[O I] λ6363	−0.31	0.92:	1.1 ± 0.3	1.5 ± 0.5	...	...	...	...	58 ± 6
[N II] λ6548	−0.34	55 ± 5	63 ± 3	96 ± 2	55 ± 8	15 ± 3	141 ± 6	129 ± 20	187 ± 9
Hα λ6563	−0.34	279 ± 1	279 ± 1	291 ± 5	328 ± 11	278 ± 6	265 ± 8	250 ± 25	278 ± 10
[N II] λ6584	−0.34	154 ± 1	190 ± 1	288 ± 5	200 ± 10	83 ± 4	440 ± 8	568 ± 20	547 ± 11
He I λ6678	−0.35	3.6 ± 0.7	4.8 ± 0.6	3.9 ± 0.8	...	7.7 ± 2	...	38 ± 10	...
[S II] λ6717	−0.36	7 ± 1	11.3 ± 1.5	20 ± 1	15.3 ± 4.5	...	28 ± 2	...	100 ± 8
[S II] λ6731	−0.36	11.4 ± 1.5	17 ± 2	26 ± 1	18.4 ± 5.5	...	28 ± 2	...	82 ± 6
$F(H\beta) \times 10^{16}$ [a]	...	1164	2790	1040	66.6	43.4	8.52	2.70	21.5

NOTE.—Colon denotes upper limit.

[a] Dereddened flux in units of ergs cm^{-2} s^{-1}.

derived from the Hγ/Hβ ratio ($E_{B-V} = 0.51$). This is an indication of self-absorption in Hβ; therefore, we adopt the $E_{B-V} = 0.46 \pm 0.01$ derived from Hα/Hγ for the extinction correction. The Balmer decrements in the other spectra are all consistent, within the error limits, with this amount of extinction. The absence of large extinction variation over the whole nebula implies that the extinction is mostly of interstellar origin. Our extinction is slightly lower than the value $E_{B-V} = 0.6$ given by Aller & Czyzak (1983), but slightly higher than the value of $E_{B-V} = 0.39$ derived from the 6 cm radio continuum and the Hβ flux (Pottasch 1984). The dereddened line strengths from each of the eight regions are presented in Table 2.

5.2. *Electron Density and Temperature*

The electron density is determined from the [S II] λ6731/λ6716 line ratio, whenever these lines are detected. When the [S II] lines have a poor signal-to-noise ratio or are not detected (in regions A, E, and H′), we assume a reasonable depth and use the Hβ flux to calculate the root mean square electron density. For the ansae, we assume its depth is the same as its width; for the envelope and the halo, we assume a spherical shell geometry.

The electron temperatures have been calculated from the [N II] line ratio (λ6548 + λ6584)/λ5755 for the low-excitation region and from the [O III] line ratio (λ4959 + λ5007)/λ4363 for the high-excitation region. In the region of C2, the [O III] electron temperature is not well determined because of the poor signal-to-noise ratio of its 4363 Å line. In region F, only [N II] electron temperature can be determined with large uncertainty; we assume an electron temperature of 8000 K for the abundance analysis below.

The derived electron densities and temperatures are listed in Table 3. Note that the electron temperature in the envelope (E) is remarkably high. Although the error in the 4363 Å line strength is somewhat large, the absence of [O II] and [S II] lines is consistent with an electron temperature nearly twice as high as that of the main nebula.

5.3. *Abundances*

After deriving the electron temperatures and densities, we compute the ionic abundances from the line strengths using a program that solves the equations of statistical equilibrium for 10-level atoms. We assume that O^0, O^+, N^+, and S^+ are from the low-excitation region, and O^{++}, S^{++}, Cl^{++}, Ne^{++}, and He^+ from the high-excitation region. The electron temperature T_e of 8000 K in the halo (H and H′) has large uncertainties. The electron temperature of the envelope (E), uncertain in itself, is adopted for the ansae (A), hence the derived abundances in the ansae may be quite uncertain. In region C2, the abundances of the high-excitation ions may be somewhat uncertain because of the large error in the [O III] electron temperature.

Element abundances are calculated using the standard formulism of ionization correction factors (Torres-Peimbert & Peimbert 1977). The ionic and elemental abundances are listed in Table 3. The helium abundances are derived with the correction of collisional effects (Clegg 1987). In the C1 spectrum, of which the signal-to-noise ratio is quite high, the He^+ abundance calculated from λ5786 agrees very well with that from λ4471, implying that the helium abundance of He/H = 0.121 is quite reliable. The total nitrogen abundance in the ansae, envelope, and halo (A, E, H, and H′) cannot be determined, because the [O II] lines are not detected, hence we cannot

TABLE 3

PHYSICAL PARAMETERS AND ABUNDANCES OF NGC 6751

Region	CS	C1	C2	A	E	H	H′	F
$\log n_e$[S II]	3.4	3.4	3.2	...	...	2.8	...	2.2
$\log n_e$[F(Hβ)]	...	...	...	2.3	1.5	...	1.3	...
t [N II]	...	0.85 ± 0.025	0.8 ± 0.025	...	...	$0.8^{+0.3}_{-0.4}$	...	$1.15^{+0.1}_{-0.1}$
t [O III]	1.15 ± 0.025	1.0 ± 0.025	0.85:	...	2.0^{+2}_{-3}	...	...	...
$O^{++}/H^+ \times 10^5$	41.6	34.1	38.3	38.5	60.6	43.9	43.5	12.4
$O^+/H^+ \times 10^5$	17.3	17.8	19.4	...	...	38.4	1.7	26.1
$O^0/H^+ \times 10^5$	1.2	1.2	3.1	...	...	...	...	10.5
$O/H \times 10^5$	60	53	61	..	61	82	45	49
$N^+/H^+ \times 10^5$	4.81	5.83	10.66	...	2.7	15.78	18.9	7.44
$N/H \times 10^5$	16.7	17.4	33.43	...	...	33.7	...	19.7
$S^+/H^+ \times 10^5$	0.097	0.146	0.285	0.02	...	0.22	...	0.30
$S^{++}/H^+ \times 10^5$	0.51	0.57	0.71	...	...	...	...	0.30
$Ne^{++}/H^+ \times 10^5$ ...	12.48	6.6	2.58	...	...	...	...	...
$Ne/H \times 10^5$	...	20	...	...	...	...	...	...
$Cl^{++}/H^+ \times 10^5$	...	0.0085	...	...	...	...	...	...
He^+/H^+(5876)	0.1195	0.1215	0.133	...	...	...	...	0.067
He^+/H^+(4471)	...	0.1210	...	...	...	...	...	...
He^+H^+(6678)	0.087	0.1155	...	...	...	...	...	...
He/H^+	0.11	0.121 ± 0.005	0.13	...	...	...	...	0.067 ± 0.03
N^+/O^+	0.28	0.33	0.55	...	...	0.4	...	0.4

NOTE.—Colon denotes upper limit.

derive the ionization correction factor for nitrogen using the relation $N^+/N = O^+/O$.

Despite the aforementioned uncertainties, two relatively firm conclusions about abundance variation in the nebula can be drawn from the results. First, the helium abundance, fairly constant within the nebula, is ~20% lower in the northeast irregular filaments. This lower abundance, closer to the solar value, is consistent with the interstellar origin of these filaments inferred from the kinematic properties.

The second conclusion concerns the variation in N/O ratio. The elemental abundance of N or O individually can have large errors, but the ratio of these two abundances is more reliable. This is because N/O can be well approximated by N^+/O^+, in which the temperature dependence of N^+ abundance nearly cancels out that of the O^+ abundance. We can see in Table 3 that the N/O ratio increases by nearly a factor of 2 from the central part (CS) and the smooth inner ring (C1) to the knotty outer ring (C2) in the main nebula. The electron temperatures from the [N II] lines are pretty well determined, and the [O II] lines are well measured for the main nebula. The error for the N/O ratio in the main nebula should be less than 10%. This variation in N/O ratio is probably real. Similar variation in the N/O ratio has been observed in NGC 7662 (Barker 1986).

It is hard to compare our results with those of Aller & Czyzak (1983), because their single-aperture observation did not resolve the features in the inner nebula as ours did. Nevertheless, we note that our helium abundance is 20% higher than theirs; our value is closer to those found in type I planetary nebulae (Peimbert & Serrano 1980).

6. DISCUSSION

6.1. *Central Star*

We can classify the central star of NGC 6751 using the spectrum shown in Figure 7*a*. Based on the ratios of line intensities (e.g., Méndez & Niemela 1981), we derive a spectral type of WC4. Using the criteria of line widths, Smith & Aller (1969) classified the star as WC6. Using the integrated Hβ flux of the nebula and the visual magnitude of the central star listed by Pottasch (1984), we derive a Zanstra temperature of 36,000 K. However, the Stoy temperature relation based on the ratio of Hβ and [O III] fluxes (Kaler & Jacoby 1991) suggests that the stellar temperature is greater than 50,000 K.

6.2. *Interaction between NGC 6751 and Its Ambient Medium*

The proximity of the H II region to NGC 6751 suggests that they share the same ionization source—the central star of NGC 6751. The radial velocity of the H II region and the velocity variation in NGC 6751 further suggest that the H II region has been interacting with NGC 6751.

A planetary nebula moving through the interstellar medium is expected to slow down, or be braked, with respect to the medium (Smith 1976; Isaacman 1979). If NGC 6751 is moving through a dense medium of which the densest part shows up as the H II region, the halo of NGC 6751 would interact directly with this medium. Since the halo is porous, the envelope gets a chance to interact with the interstellar medium, too. Both components should show some deceleration from the systemic velocity of $V_{hel} = -42 \pm 2$ km s^{-1} exhibited in the main nebula. Indeed, the ring of knots in the halo, being the oldest, has been braked the most and its average velocity is $V_{hel} = -35$ km s^{-1}. The envelope shows deceleration, too; as seen in Figures 4 and 5, the line image of the static envelope is curved toward more positive velocities at the edges. The southern edge of the envelope has a radial velocity of $V_{hel} = -38$ km s^{-1}.

Unfortunately, we cannot model the braking quantitatively, since the density in the ambient medium is unknown. Nevertheless, the velocity variation supports qualitatively that NGC 6751 is indeed moving through the interstellar medium and being braked by the medium.

Distances to planetary nebulae have always been quite uncertain (Lutz 1989). Since NGC 6751 is physically associated with an H II region, we have an additional way of determining its distance: using the radial velocity of the H II region to derive a kinematic distance. Assuming a flat rotation curve at 220 km s^{-1} and assuming a distance of 8 kpc from the Sun to

TABLE 4

MASSES AND MASS-LOSS RATE OF NGC 6751[a]

Region	Diameter	ϵ	Mass ($M_\odot$)	V_{exp} (km s^{-1})	R (pc)	t (yr)	$\dot{M}$ ($M_\odot$ yr^{-1})
Main nebula	25″	0.06	0.017	42.5	0.12	2700	2.2×10^{-5}
Knots	...	1	0.004	...	...	...	...
Ansae	4	1	0.002	...	0.02	...	...
Envelope	48.3	1–0.02	0.068–0.007	10	0.23	28500	$(2.7–26) \times 10^{-7}$
Halo	87.4	0.0037	0.016	7	0.42	63400	4.6×10^{-7}
H II	...	0.075	0.021	7	...	...	...

[a] $d = 2$ kpc.

the Galactic center, we derive a distance of 2.0 kpc to NGC 6751. This distance is similar to, but smaller than, the 2.7 kpc derived by Maciel & Pottasch (1980) and by Daub (1982).

6.3. *Physical Structure of NGC 6751*

We use the information on the morphology, kinematics, and abundance variation in NGC 6751 to model its physical structure. For clarity, we list the size, expansion velocity, and dynamical age of each morphological feature in Table 4. A schematic drawing of our model of NGC 6751 is given in Figure 8.

The main nebula is a thick shell with a velocity gradient within the shell, and the bulk expansion velocity is $\sim$42 km s^{-1}. The embedded [N II] knots near the periphery have higher N/O than the shell, indicating a separate mode of mass loss from the central star. The ansae correspond to a bipolar mass outflow. If this outflow started out from the star, it would have lasted only a short period of time, as opposed to the continuous jet in the Eskimo nebula (Gieseking, Becker, & Solf 1985), where the bipolar material is detected from the periphery to the star. The juxtaposition of the ansae to the periphery of the main nebula may also imply that the outflow is accelerated interior to the shell instead of near the star. The envelope has a slow expansion velocity. Its high excitation is hard to understand, since its velocity profiles are narrow, implying small turbulences. Shock excitation is not likely. The halo is so tenuous that only the condensations are seen. The halo may be quite porous, since the interstellar material apparently sieves through the halo to interact with the envelope.

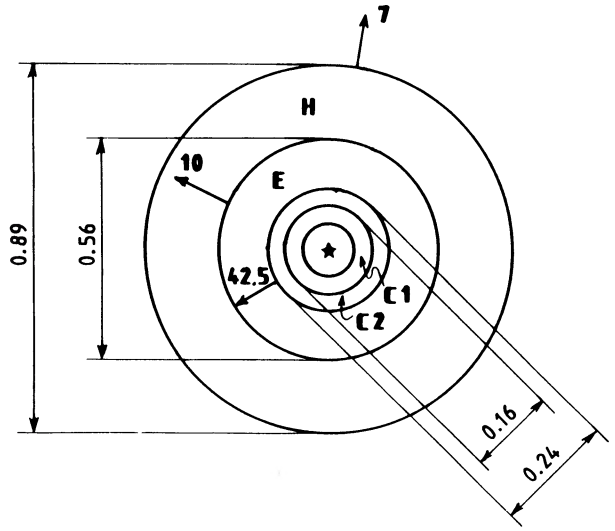

FIG. 8.—Proposed model for NGC 6751. Dimensions of each region are in parsecs (at the adopted distance of 2 kpc). Numbers in thick outline associated with the arrows indicate the expansion velocity in km s^{-1}.

We adopt the kinematic distance of 2 kpc for NGC 6751. Knowing the expansion velocity and linear size, we can compute the dynamic age of each shell, approximated as (radius)/(expansion velocity). This approximation is probably uncertain by a factor of 2 or more, since neither a deceleration nor an acceleration mechanism has been taken into account. All shells have been decelerated by the slower material outside, but the innermost shell has also been accelerated by the fast stellar wind from within. The approximate dynamic ages are listed in Table 4.

6.4. *History and Properties of Mass Loss*

Planetary nebula nuclei can lose mass in many ways. The triple-shell structure of NGC 6751 clearly cannot be explained by the popular "two-wind interaction model," in which a tenuous stellar wind with a terminal velocity of 2000–3000 km s^{-1} sweeps up the envelope of previous slow wind (Kwok, Purton, & FitzGerald 1978; Balick 1987). From the physical structure of NGC 6751, we see chronologically the following episodes of mass loss: (1) isotropic slow ($<$10 km s^{-1}) wind started 64,000 years ago, but the duration of this episode is unknown; (2) another isotropic slow ($\sim$10 km s^{-1}) wind started 28,000 years ago, and lasted until 3200 years ago, when the next episode of faster mass loss started to form the main nebula; (3) the ansae were formed by a short duration of a bipolar ejection at an unknown time (because the inclination angle of the ansae is unknown); (4) a ring of N-rich material was ejected; (5) a faster mass loss started about 3200 years ago to form the main nebula that is expanding at $\sim$42 km s^{-1}. We stress again that these ages may be uncertain by a factor of 2 or more.

We can analyze the shell structure quantitatively from the Hβ fluxes and the electron densities determined from the [S II] lines. We may either assume a depth along the line of sight and calculate the filling factor or assume a filling factor of unity and calculate the depth. From the density, volume, and filling factor, the mass can be derived. From the mass and the duration of the shell formation, we can calculate an approximate stellar mass-loss rate.

For the main nebula we obtain a filling factor of 0.017, using the spectrum CS and assuming a depth equal to the diameter of 25″. This filling factor is much smaller than the ratio of the apparent shell thickness to the shell radius of the main nebula. The shell thickness can be approximated as the spatial extent over which the line profiles are not split, or the spatial width of

the line image at the systemic velocity. From Figure 3, we see an apparent shell thickness of 3″–4″, which is about 25%–30% of the radius. Therefore, the filling factor in the shell must be only 6%–7%. The mass in the shell of the main nebula is about 0.017 $M_\odot$.

The spectrum C2 corresponds to the [N II] knots. Using the electron density and Hβ flux, we derive a depth of about 1″ for a unity filling factor. This depth is of order similar to the widths of the knots, indicating that these knots are indeed three-dimensional ones. The mass of each knot is about 0.00025 $M_\odot$. We count about 15–20 knots in Figure 1; their total mass would be about 0.004 $M_\odot$.

The small filling factor in the outer halo (H), 0.0037, implies a very porous structure. Only the densest spots in the outer halo are visible. The total mass in this halo is about 0.016 $M_\odot$.

The electron density in the static envelope cannot be determined, since the [S II] lines were not detected. Assuming a unity filling factor, we may derive a root mean square density of about 30 cm^{-3}, and a total mass of about 0.068 $M_\odot$ in the static envelope. If the filling factor is similar to that in the main nebula, the mass would be about 0.015 $M_\odot$; if the filling factor is as small as that in the outer halo, the mass would be about 0.007 $M_\odot$.

For the irregular filaments (F), we use the width as the depth along the line of sight and derive a filling factor of 0.075. This filling factor is consistent with those commonly seen in the interstellar medium.

Knowing the mass and dynamic age of each shell, we may estimate the average mass-loss rate during the formation of each shell. We make an a priori assumption that there is no gap from one episode of mass loss to the next. The duration of the mass loss for the halo would be the dynamic age of the halo minus the dynamic age of the envelope, that of the envelope would be the age of the envelope minus the age of the main nebula, and that of the main nebula is the age difference between the outer and inner shell surfaces. We derive average mass-loss rates of 4.6×10^{-7} $M_\odot$ yr^{-1} for the halo, (3–26) $\times 10^{-7}$ $M_\odot$ yr^{-1} for the envelope, and 2.2×10^{-5} $M_\odot$ yr^{-1} for the main nebula. These mass-loss rates can be compared to those of OH/IR stars, a few times 10^{-6} to a few times 10^{-4} $M_\odot$ yr^{-1} (Habing, te Lintel Hekkert, & van der Veen 1989). The agreement is reasonable within the uncertainties.

We may also derive the nebular mass from the *IRAS* far-IR fluxes (Phillips & Mampaso 1988). Adopting Draine's (1990) grain emissivity, we derive a dust mass of 0.001 $M_\odot$. If we assume a dust-to-gas ratio of 0.01, the nebular mass is 0.1 $M_\odot$, consistent with the total mass of 0.05–0.1 $M_\odot$ derived from the electron densities and Hβ fluxes. Changing the adopted distance from 2 to 2.7 kpc will increase the ages and the mass-loss rates by a factor of 1.35, and the masses by a factor of 1.82.

6.5. *Abundance Variations*

As described in § 5.3, there are variations in the He/H and N/O ratios in NGC 6751. The He/H ratio variation is between the planetary nebula and the ambient interstellar medium. The He/H ratio within the planetary nebula itself is pretty constant. The N/O ratio variation, on the other hand, is within the planetary nebula. The N/O ratio is a factor of 2 higher in the knotty outer ring in the main nebula (C2) than the other places in the nebula. This N/O ratio variation could be due to different phases in the dredge-up process. The observed N/O and He/H ratios can be compared to the theoretical predictions of nucleosynthesis models after the second and third dredge-up phases (Becker & Iben 1980); the abundances in the knotty outer ring (C2) match well the second dredge-up, and those of the smooth inner ring of the main nebula (C1) match well with the third dredge-up.

6.6. *Comparison with Other Triple-Shell Nebulae*

There are seven known triple-shell nebulae. A78 is a reborn planetary nebula that clearly has a different evolutionary status (Iben et al. 1983) than the other nebulae. We will therefore discuss only the other six nebulae. For convenience, we call the outermost shell "halo," and the inner two shells "outer shell" and "inner shell."

Morphologically, NGC 2022, NGC 6826, NGC 6891, and NGC 7662 all have type II double-shell structure in the inner two shells, with the outer shell being about 20% as bright as the inner shell, while NGC 6720 has a type I double-shell structure in the inner shells, with the outer shell being less than 0.5% as bright as the inner shell (CJA). The two inner shells of NGC 6751 are intermediate between these two types; its outer shell (the envelope) is about 1%–2% as bright as the inner shell (the main nebula).

Kinematically, NGC 6751 is the only triple-shell nebula that has two shells (the halo and the envelope) expanding subsonically. NGC 2022 and NGC 7662 have the outer shell expanding at a velocity similar to that of the inner shell; NGC 6826 and NGC 6891 have the outer shell expanding faster than the inner shell; and NGC 6720 has the outer shell expanding slower than the inner shell (Chu 1989). All of these five nebulae have the two inner shells expanding supersonically. If the subsonically expanding shells are the mass lost by the progenitor red giant's wind, the envelope and halo of NGC 6751 give clear evidence that the red giant wind may go through sudden change in velocity and mass-loss rate.

7. SUMMARY

We have studied the morphology, internal motion, and physical condition of the triple-shell planetary nebula NGC 6751. The main nebula of NGC 6751 is expanding at about 42 km s^{-1}. The [N II]–bright knots embedded in the periphery of the main nebula may follow a different pattern of expansion, and they have a higher N/O ratio than the other parts of the nebula. The bipolar mass outflow corresponds to the pair of ansae at position angles of 104° and 284°. The ansae and the main nebulae are inside an oval whose relationship to the rest of the nebula is unknown. The envelope has a small expansion velocity ($\sim$10 km s^{-1}), but its electron temperature is very high, nearly twice the temperature in the main nebula. The halo is porous, and its expansion velocity is lower than 7 km s^{-1}.

The shell structure of NGC 6751 gives clear evidence that the progenitor of the PN nucleus must have gone through mass loss in a complex way. The mass in each shell is about 0.01–0.02 $M_\odot$, and the mass-loss rate increases from a few times 10^{-7} $M_\odot$ yr^{-1} during the formation of the halo to a few times 10^{-5} $M_\odot$ yr^{-1} during the formation of the main nebula.

The irregular filaments to the northeast of NGC 6751 are very likely interstellar material illuminated by the central star of NGC 6751. The radial velocity of this H II region is different from that of the planetary nebula by 55 km s^{-1}, and the He/H ratio is lower in the H II region. NGC 6751 is apparently moving through a dense interstellar medium, of which the densest part shows up as the H II region, and the halo has experienced braking from this medium.

Y. H. C. acknowledges the support of NSF grant AST-8818192.

REFERENCES

Aller, L. H., & Czyzak, S. J. 1983, ApJS, 51, 211
Balick, B. 1987, AJ, 94, 671
Balick, B., Preston, H. L., & Icke, V. 1987, AJ, 94, 1641
Barker, Y. 1986, ApJ, 308, 314
Becker, S. A., & Iben, I. 1980, ApJ, 237, 111
Chu, Y.-H. 1989, in IAU Symposium 131, Planetary Nebulae, ed. S. Torres-Peimbert (Dordrecht: Kluwer), 105
Chu, Y.-H., Jacoby, G. H., & Arendt, R. 1987, ApJS, 64, 529 (CJA)
Clegg, R. E. S. 1987, MNRAS, 229, 31P
Daub, C. T. 1982, ApJ, 260, 612
Dekker, H., & D'Odorico, S. 1985, Faint Object Spectrograph and Camera Operational Manual (Garching: ESO)
Draine, B. T. 1990, in The Interstellar Medium in Galaxies, ed. H. A. Thronson & J. M. Shull (Dordrecht: Kluwer), 483
Duncan, J. C. 1937, ApJ, 86, 496
Gieseking, F., Becker, I., & Solf, J. 1985, ApJ, 295, L17
Gieseking, F., & Solf, J. 1986, A&A, 163, 174 (GS)
Habing, H. J., te Lintel Hekkert, P., & van der Veen, W. E. C. J. 1989, IAU Symposium 131, Planetary Nebulae, ed. S. Torres-Peimbert (Dordrecht: Kluwer), 359
Hua, C. T., & Louise, R. 1990, A&A, 235, 403
Iben, I., Jr., Kaler, J. B., Truran, J. W., & Renzini, A. 1983, ApJ, 264, 605
Isaacman, R. 1979, A&A, 77, 327
Kaler, J. B., & Jacoby, G. H. 1991, ApJ, 372, 215
Kwok, S., Purton, C. R., & FitzGerald, M. P. 1978, ApJ, 219, L125
Lutz, J. H. 1989, in IAU Symposium 131, Planetary Nebulae, ed. S. Torres-Peimbert (Dordrecht: Kluwer), 65
Maciel, W. J., & Pottasch, S. R. 1980, A&A, 88, 1
Manchado, A., Pottasch, S. R., & Mampaso, A. 1988, A&A, 191, 128
Méndez, R. H., & Niemela, V. S. 1981, in IAU Symposium 99, Wolf-Rayet Stars: Observations, Physics, Evolution, ed. C. W. H. de Loore & A. J. Willis (Dordrecht: Reidel), 457
Moreno, M. A., & López, J. A. 1987, A&A, 178, 319
Peimbert, M., & Serrano, A. 1980, Rev. Mexicana Astr. Af., 5, 9
Phillips, J. P., & Mampaso, A. 1988, A&A, 190, 237
Pottasch, S. R. 1984, Planetary Nebulae (Dordrecht: Reidel)
Smith, H. 1976, MNRAS, 175, 419
Smith, L. F., & Aller, L. H. 1969, ApJ, 157, 1245
Torres-Peimbert, S., & Peimbert, M. 1977, Rev. Mexicana Astr. Af., 2, 181
Walsh, J. R., & Meaburn, J. 1987, MNRAS, 224, 885